Configurable Resistive Switching between Memory and Threshold Characteristics for Protein-Based Devices

Hong Wang, Yuanmin Du, Yingtao Li, Bowen Zhu, Wan Ru Leow, Yuangang Li, Jisheng Pan, Tao Wu, and Xiaodong Chen**

The employ of natural biomaterials as the basic building blocks of electronic devices is of growing interest for biocompatible and green electronics. Here, resistive switching (RS) devices based on naturally silk protein with configurable functionality are demonstrated. The RS type of the devices can be effectively and exactly controlled by controlling the compliance current in the set process. Memory RS can be triggered by a higher compliance current, while threshold RS can be triggered by a lower compliance current. Furthermore, two types of memory devices, working in random access and WORM modes, can be achieved with the RS effect. The results suggest that silk protein possesses the potential for sustainable electronics and data storage. In addition, this finding would provide important guidelines for the performance optimization of biomaterials based memory devices and the study of the underlying mechanism behind the RS effect arising from biomaterials.

1. Introduction

Natural biomaterials are of growing interest with respect to the fabrication of solid-state electronic devices, as the created electronic components are typically biocompatible, biodegradable, sustainable, and even metabolizable.[1–7] In addition, solid-state devices provide an ideal approach for the exploration of electron transfer processes within biomaterials, which are among the most fundamental processes in biological systems and crucial for various biological energy conversion processes.[8] Besides these values, biomaterials are widely available, cost-competitive, light-weight, and capable of large area fabrication on flexible substrates.[9,10] As of now, biomaterials have been employed in the building of functional solid-state devices such as transistors, diodes, and optical waveguides.[9–18] Recently, the demands of future green information storage have triggered the development of natural biomaterials based memory devices.[19,20] Among several types of memory, resistive switching (RS) memory devices, in which the resistance can be switched between a high resistance state (HRS) and a low resistance state (LRS) through an applied electrical field, have received significant research interest due to its simple structure, low cost, and excellent scalability.[21–52] Biomaterials, such as DNA and protein, have been demonstrated to exhibit RS characteristics.[53–61] However, the tunability of biomaterials based RS devices between nonvolatile and volatile states, which plays a vital role in the utilization of RS devices, remains a challenge with respect to fulfilling the demands of sustainable electronic devices.

Normally, the RS effect of memory devices can be divided into two categories based on volatility, namely memory RS (nonvolatile) and threshold RS (volatile).[62–65] Memory RS is characterized by the preservation of stability in both HRS and LRS with the absence of external voltage (**Figure 1**a), while in threshold RS, only the HRS is stable when no external bias is applied (Figure 1b). The difference in both types of RS effects delivers great diversity and significant advantages in the selection of RS devices for practical applications. For instance, memory RS can realize nonvolatile data storage while threshold RS can be employed as a selector to solve the sneak path problem in cross-bar for high density memory applications.[66] Therefore, it is of technological importance to control the type of RS devices with respect to the two modes.

In this work, we report for the first time the fabrication of configurable RS device based on silk protein. It was found that the silk protein based devices exhibit memory RS behavior with a high compliance current (100 μA) in the set process, and threshold RS behavior with a low compliance current (10 μA). In this way, the types of RS manifested by the device can be effectively and precisely controlled. Furthermore, both

Dr. H. Wang, Dr. Y. Li, B. Zhu, W. R. Leow, Prof. X. Chen
School of Materials Science and Engineering
Nanyang Technological University
50 Nanyang Avenue, Singapore 639798, Singapore
E-mail: chenxd@ntu.edu.sg
Dr. H. Wang
School of Advanced Materials and Nanotechnology
Key Laboratory of Wide Band Gap
Semiconductor Technology
Xidian Univeristy
Xi'an 710071, China
Dr. Y. Du, Prof. T. Wu
Solar and Photovoltaics Engineering Research Center
King Abdullah University of Science and Technology
Thuwal 23955-6900, Kingdom of Saudi Arabia
E-mail: tao.wu@kaust.edu.sa
Dr. Y. Li
School of Physical Science and Technology
Lanzhou University
Lanzhou 730000, China
Dr. J. Pan
Materials Centre of Innovation
Institute of Materials Research and Engineering
3 Research Link, Singapore 117602, Singapore

DOI: 10.1002/adfm.201501389

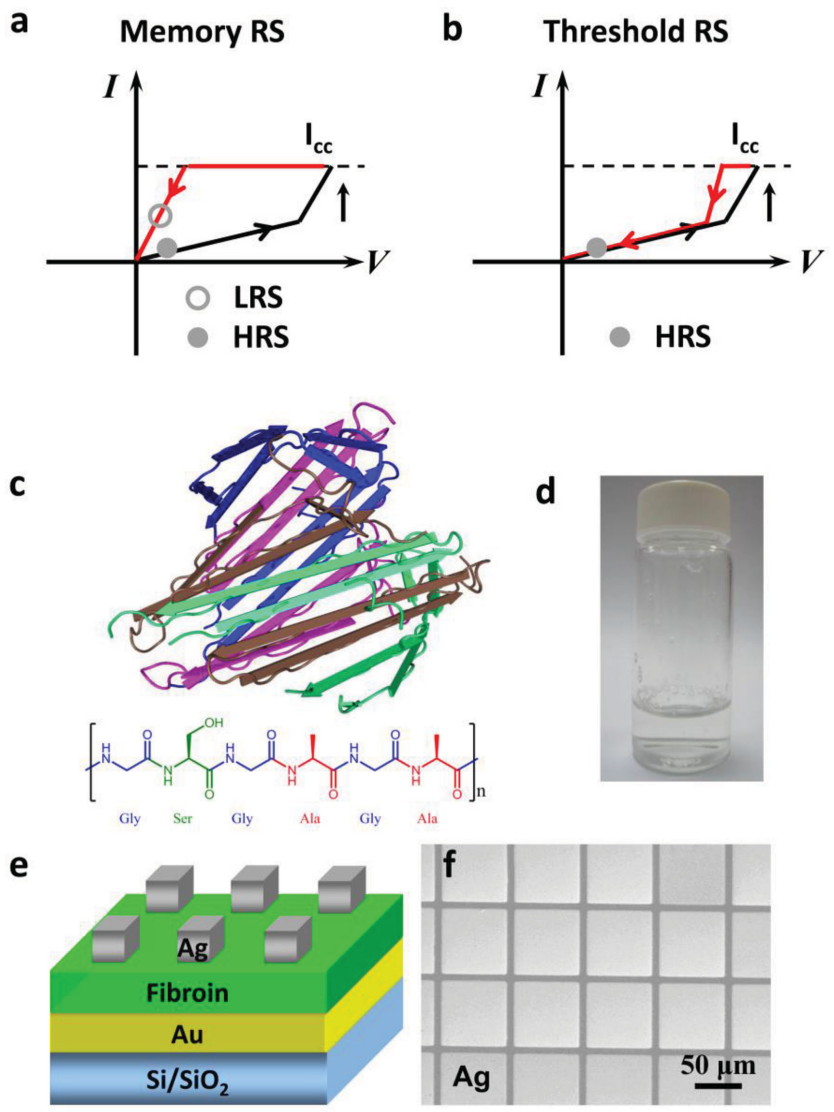

Figure 1. Schematic diagrams of *I–V* curves for the two resistive switching (RS) effects: a) memory RS and b) threshold RS. Memory RS manifested as two resistance states without applied voltage: low resistance state (LRS) and high resistance state (HRS). Meanwhile, threshold RS comprises only HRS without applied voltage. The dashed lines on the RS represent the set compliance current. c) Structure of fibroin. Top: secondary structure of *N*-terminal domain fibroin. Bottom: primary structure of fibroin. d) Optical images of the aqueous solution of fibroin. e) Schematic of the fabricated resistive switching device with a Ag/fibroin/Au configuration. f) SEM image of the fabricated device arrays.

types of protein-based devices present functionality of random access memory, and read-only memory can be achieved with the memory RS effect. This finding would provide important guidelines for the performance optimization of biomaterials based memory devices and the study of the underlying mechanism behind the RS effect arising from biomaterials.

Silk that comprises two kinds of proteins, namely fibroin and sericin,[56] was selected as the functional material in our RS devices due to the following reasons. First, as silk has already been widely studied for applications in electronic and optoelectronic devices,[12–18] further development in devices of different functions would be helpful toward simplifying the integrated technology for future silk-based electronics. Second, silk is among the most representative of proteins that have shown RS effect;[55,56] hence, development in on-demand RS devices and understanding of the RS effect based on silk would pave the way for future improvement of protein-based memory technology.

2. Results and Discussion

In our fabrication process, the fibroin aqueous solution (Figure 1c,d) used was derived from *Bombyx mori* cocoons in accordance with a previously reported procedure.[13] The simple metal–insulator–metal (MIM) cell structure (as illustrated in Figure 1e) was employed for investigating the RS effect. In a typical experiment, a 50 nm Au film with 3 nm Cr adhesion layer was thermally deposited on a SiO_2/Si substrate to act as the bottom electrodes. Next, approximately 120 nm fibroin film was spin-coated onto the Au electrodes as the RS layer. Finally, the top Ag electrodes with an area of 80 × 80 μm^2 (Figure 1f) were thermally deposited and patterned by a shadow mask.

The RS characteristics of the fibroin-based RS device were then investigated. **Figure 2**a shows the typical current–voltage (*I–V*) curves of the fibroin-based device under a direct current sweeping mode, measured by applying voltage to the top Ag electrode while keeping the Au bottom electrode grounded. As the voltage sweeps from zero to a positive voltage, a sharp increase in current can be observed at a certain voltage, during which the device switches from HRS to LRS, which is denoted as the set process. Interestingly, control of the type of RS can be achieved by controlling the compliance current (I_{cc}) in the set process; for example, memory RS can be triggered by setting I_{cc} = 100 μA, while threshold RS can be triggered by setting I_{cc} = 10 μA. For memory RS, without setting the I_{cc}, the device can be switched back to HRS during the sweep from zero to a negative voltage through the reset process. In this way, the controlled and reversible alternation between memory and threshold RS in a single device is realized (Figure 2b).

To understand the two types of RS effects, the RS characteristics of the fibroin-based devices were systematically studied with different compliance currents in the set process. All devices displayed memory RS effect with compliance current between 100 μA and 10 mA, as seen from the *I–V* curves in **Figure 3**a–1 (I_{cc} = 10 mA), Figure S1a (I_{cc} = 100 μA) and Figure S2a (I_{cc} = 1 mA) (Supporting Information). It is worth noting that resistance of LRS decreases with increasing compliance

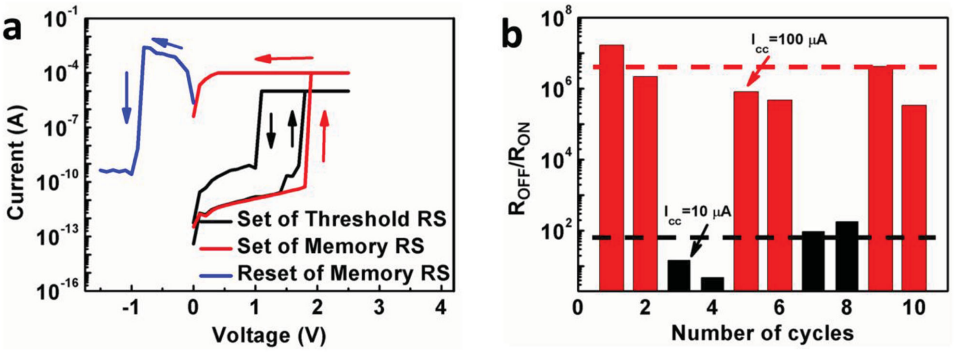

Figure 2. a) The *I–V* curves of the RS behaviors of the Ag/fibroin/Au device. The threshold RS, memory RS, and the reset processes were achieved by setting the device at different compliance currents. b) Switching between memory and threshold behaviors in a series of cycles. The R_{OFF} and R_{ON} were read at voltage of 100 mV in forward and reverse sweeping, respectively. The dash lines represent the average R_{OFF}/R_{ON} ratio.

current, while that of HRS shows no obvious dependence on the compliance currents (the device-to-device distributions of HRS and LRS resistances are shown in Figures 3a-2, S3, and S4 in the Supporting Information). The HRS resistance ranges from 3.5×10^8 to 9.3×10^{10} Ω, while the LRS resistance ranges from 18 to 35 Ω, 70 to 147 Ω, and 423 to 3760 Ω under the 10 mA, 1 mA, and 100 μA set compliance currents, respectively. Under the 10 mA set compliance current, resistance OFF/ON ratios as large as 10^7 can be achieved (Figure 3a-2). The set and reset voltages range from 1.3 to 3.4 V and –0.5 to –1.3 V, respectively (the device-to-device distributions of set and reset voltage are shown in Figure S5 in the Supporting Information), and they are independent of the compliance current. To evaluate the memory performance of the fibroin-based

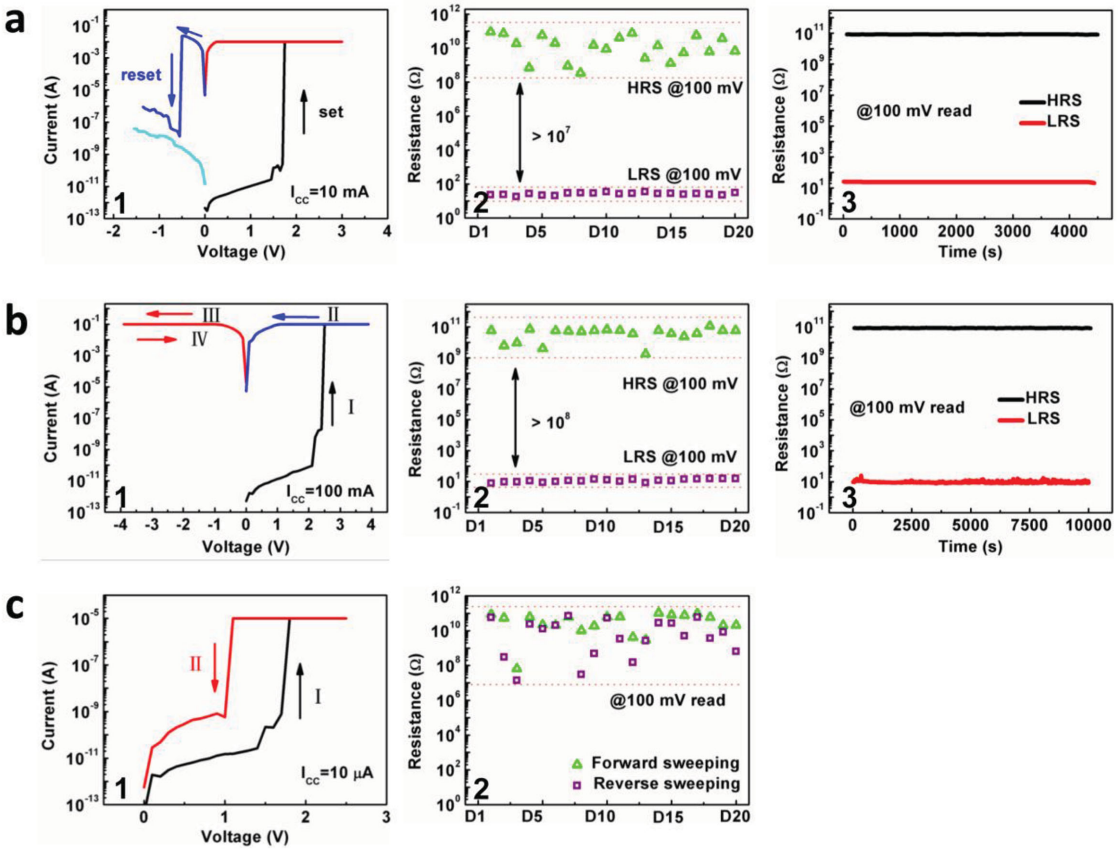

Figure 3. The RS characteristics of the device under the set compliance current of a) 10 mA, b) 100 mA, c) 10 μA, in which 1) shows the typical *I–V* curves of the device; 2) shows the device to device distributions of the resistance of HRS and LRS a,b), the resistance during forward and reverse sweeping c), the results were obtained under a 100 mV read voltage from 20 devices; and 3) shows the retention characteristics of the device under a 100 mV readout voltage at room temperature.

RS device, the retention characteristic was measured under 100 mV read voltage at room temperature. The resistance of HRS was discovered to be very stable, while the stability of LRS depended on the set compliance current; LRS retention time is about 1100 and 1500 s with 100 μA and 1 mA set compliance currents, respectively (Figures S1b and S2b, Supporting Information). At a higher compliance current of 10 mA, the retention characteristic can be further improved with the resistance of LRS displaying no obvious change for more than 4500 s (Figure 3a-3). To sum up, we have successfully achieved a high-performance memory RS device based on fibroin with OFF/ON ratio of 10^7 and retention time of more than 4500 s, which is potentially suitable for nonvolatile random access memory applications. More importantly, this study may open the door toward optimizing the performance of biomaterial-based RS memory devices.

The study conducted on the RS characteristics of the fibroin-based devices at the set compliance current of 100 mA, as seen from the typical *I*–*V* curves in Figure 3b-1, is also of great significance. Similar to that of the aforementioned compliance currents, sweeping the voltage from zero to positive up to the set voltage resulted in the device switching from HRS to LRS (stage I in Figure 3b-1), which is sustained in the subsequent sweep from zero to a positive voltage (stage II in Figure 3b-1). However, what sets it apart from the aforementioned set compliance currents is that the device cannot be switched back to HRS (stages III and IV in Figure 3b-1), which makes it potentially useful for application as a write-once read-many-times (WORM) memory element.[67] The device-to-device distributions of HRS and LRS resistances of the WORM memory devices range from 1.7×10^9 to 1.1×10^{11} Ω and 8 to 15 Ω, respectively (Figure 3b-2), indicating that high resistance OFF/ON ratios as large as 10^8 can be achieved in fibroin-based WORM memory devices. The achieved OFF/ON resistance ratio is larger than that of the previously reported WORM memory devices based on biomaterials,[53] which generally implies a lower misreading rate during read operation. A retention test was conducted in both HRS and LRS to evaluate the stability of data storage in the fibroin-based WORM memory device (Figure 3b-3). It can be observed that no significant change in resistance occurred at either state for more than 10^4 s. This is strong evidence that our fibroin-based RS device is also suitable for high-performance WORM memory applications.

In order to elucidate the threshold RS behavior of the fibroin-based devices, a study was conducted on the RS characteristics of the devices at the low set compliance currents of 10 μA, 1 μA, and 100 nA. Figure 3c shows the *I*–*V* curves of the fibroin-based RS devices at the set compliance current of 10 μA. All the devices display threshold RS with set compliance currents in the range of 100 nA to 10 μA, which is conclusive evidence that we have successfully fabricated a configurable RS device based on fibroin. It is significant that the RS effect of such devices can be effectively controlled between memory and threshold RS by defining the compliance current in the set process. WORM memory can be realized at the set compliance current of 100 mA, while random access memory can be obtained under the set compliance currents ranging from 100 μA to 10 mA. The devices were also able to demonstrate the threshold RS behavior under set compliance currents within the range of 100 nA to 10 μA.

We have also attempted to clarify the mechanism of the RS effect of the fibroin-based device. The electrolytic migration of Ag atoms and clusters in an insulator matrix is one of the most common phenomena in electronics, which leads to the formation of metallic filaments in resistive switching devices.[21,68,69] The transition between HRS and LRS states can be explained by fracturing and reformation of the Ag filaments embedded in the insulating layer. To further understand the resistive switching mechanism, we performed temperature-dependent resistance measurements for both LRS and HRS states (Figure S6, Supporting Information). Interestingly, a nonmetallic behavior was observed in the LRS measurement, with characteristic similar to that shown in the HRS, that is, the resistance decreases with increasing temperature. This indicates that the LRS is not dictated by metallic Ag filaments, and both HRS and LRS could come from the same mechanism. To explain this behavior, we propose that instead of Ag filaments, Ag nanoparticles are formed in the insulator layer during the electrode deposition and electroforming processes of the device,[48] which is consistent with the secondary ion mass spectrometry (SIMS) analysis results (Figure S7, Supporting Information). Through charge trapping and detrapping processes, hopping of electrons between Ag islands contributes to the current flow (**Figure 4**a,b). If this scenario is correct, the voltage-dependent *I*–*V* characteristic for both states should follow that of an insulator with traps and space-charge-limited (SCL) current injection. In terms of the SCL conduction, the *I*–*V* curve first follows the Ohm's law at low bias and then the Child's law at high bias

$$J \propto \frac{9}{8}\varepsilon_0\varepsilon_r\,\mu\frac{V^2}{d} \tag{1}$$

where J is the current density, ε_0 is the permittivity of free space, ε_r is the relative dielectric constant, μ is the mobility of charge carriers, V is the voltage, and d is the film thickness.[70] The *I*–*V* curves for both resistance states are drawn in the log–log scale in Figure 4c. Indeed, for the LRS (inset of Figure 4c), an Ohmic behavior ($I \propto V$) is followed by a SCL behavior ($I \propto V^2$), suggesting a change from the trap-unfilled SCL conduction to the trap-filled SCL conduction. The HRS also shows an Ohmic behavior at lower voltages, while a larger slope (≈3) emerges in the higher voltage range. The increase of the slope could be due to the density and energy distribution of the traps.[71,72]

When a positive voltage is applied to the top electrode of the MIM capacitor structure, positive charges are created at the top interface, with a negative charge zone screened at the bottom interface. This leads to a high electrical field at both interfaces (Figure S8a, Supporting Information). Anodic dissolution of Ag atoms occurs according to the reaction

$$\mathrm{Ag} \rightarrow \mathrm{Ag}^+ + e^- \tag{2}$$

The DC electric field between anode and cathode will cause the Ag^+ ions to migrate across the fibroin layer. With the incoming electrons from the cathode side, the cations will be reduced during the electro-migration process (Figure S8b,

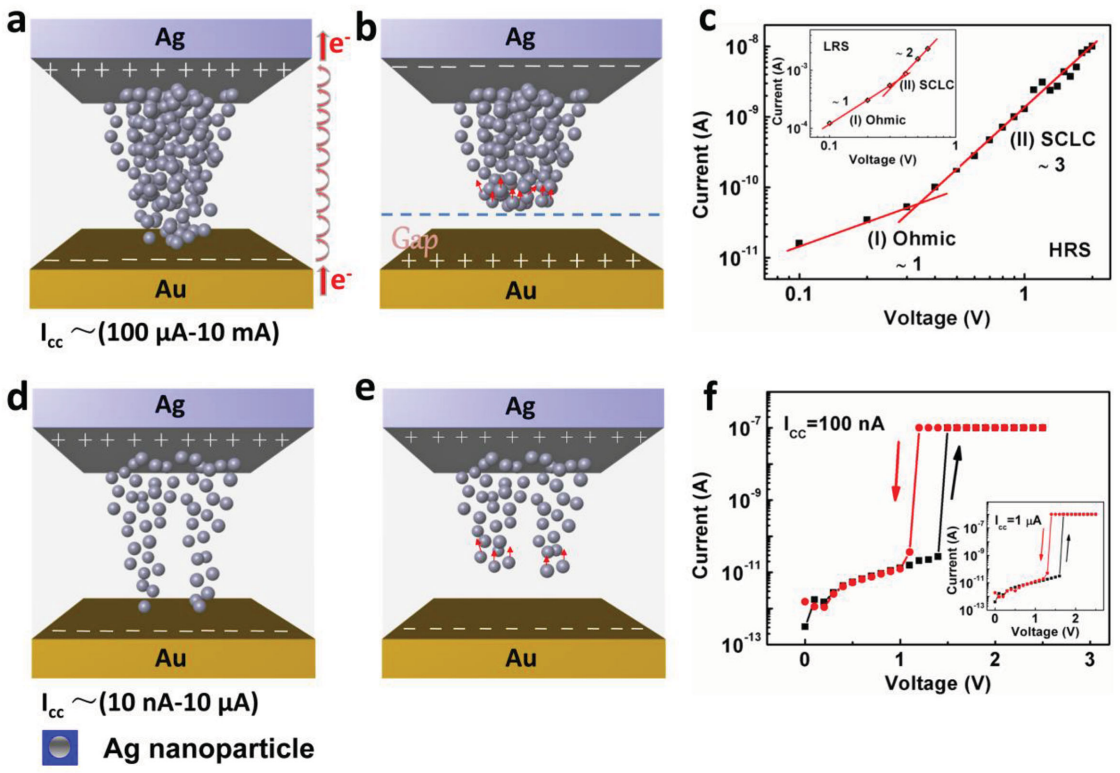

Figure 4. a–c) Operation mechanism of the memory RS effect. a) Schematic of the device at the ON state with electrons hopping through Ag nanoparticles within the fibroin layer formed after an electro-migration process. Charges with different polarities are accumulated at the two electrode/fibroin interfaces when a positive voltage is applied to the top electrode. b) Schematic of the OFF state with a large tunneling gap formed when a negative voltage is applied to the top electrode. The distributions of charges are also changed as a result of the applied voltage. c) *I–V* curve in a log–log scale of the OFF state. The inset shows the *I–V* curve of the ON state. d–f) Operation mechanism of the threshold RS effect. d) Fewer electron hopping paths are formed under a lower compliance current, although the charge accumulation is similar to the case of (a) when a positive voltage is applied. e) The decrease of the voltage leads the device back to the OFF state. f) *I–V* curve in a semi-log scale under an I_{cc} of 100 nA. The inset shows the *I–V* curve under an I_{cc} of 1 μA.

Supporting Information). The cation mobility of the Ag ions could be enhanced by the local Joule heating under high current, and a high electrical field is effective to accelerate the electro-migration process.

Figure 4a shows the schematic of LRS after a higher I_{cc} electro-forming process. Different to the often cited metallic filament conduction, electrons hopping through the silver islands leads to the high current at the ON state. The removal of the electrical field would terminate the charge injection and result in a neutralized state, as shown in Figure S8c (Supporting Information). Figure 4b shows the HRS with a negative voltage applied to the top electrode. Anodic dissolution of Ag atoms and formation of a positively charged zone occur at the bottom interface. Due to the Coulomb repulsion effect, the Ag^+ ions will be pushed back, and as a result, a large tunneling gap is formed after such a process. The proposal of "broken" silver chains at the bottom interface is consistent with the report by Yang et al.[73] Furthermore, the interface-modulated resistive switching has been widely reported.[74–76] The number of electron hopping paths is significantly reduced after such a reset process, which results in the OFF state (HRS). After the removal of the negative electrical field, a neutralized state could be formed for the HRS state, as shown in Figure S8d (Supporting Information).

This mechanism of dynamic Ag nanoparticle ensembles in the fibroin layer is also helpful to elucidate the threshold RS behavior of the RS devices, for which a lower set compliance current was applied. In comparison to the memory state formation under a higher I_{cc} (Figure 4a,b), we propose that only a very small number of conductive channels are formed (Figure 4d), as a result of less Ag ions and clusters migrating under a much lower I_{cc}. This is consistent with the much higher resistance of the ON state (HRS), compared to that of the nonvolatile memory switching. Due to the screening effect, the repelling between silver ions at the bottom interface leads to an OFF state shown in Figure 4e, which means that the resistance almost comes back to the original state. The *I–V* curves plotted in the semi-log scale are shown in Figure 4f. The current first increases to the I_{cc} and then significantly drops with decreasing voltage. The difference between memory and threshold switching is a result of the formation of conductive (hopping) paths of Ag nanoparticles in our devices. For the memory RS, resistance of different LRS states decreases with increasing I_{cc} (from 100 μA to 10 mA), indicating more and more conductive paths formed during the electro-migration process. In comparison, the results shown in Figure 3c imply an unsuccessful formation of conductive paths in the fibroin film when a lower I_{cc} of 10 μA is used. We also performed

a measurement with a higher I_{cc} at 50 μA (Figure S9a, Supporting Information), and the result reveals the unstability of the conducting paths in the LRS. With such low I_{cc}, the measured LRS was unstable and degraded to an OFF state after tens of seconds (Figure S9b, Supporting Information). On the other hand, a stable resistive switching with good retention behavior can be achieved by further increasing the I_{cc} to 100 μA (Figure S1, Supporting Information).

In WORM memory obtained with a very high set compliance current of 100 mA, the LRS cannot be switched back to HRS. Figure S10 (Supporting Information) shows the *I–V* curve of LRS, with the set I_{cc} at 100 mA. Interestingly, the fitting of the curve in the whole voltage range shows a consistent linear characteristic. The I_{cc} of 100 mA is much higher than the set I_{cc} values used for achieving memory RS; thus, we can expect a more sufficient migration of silver ions and clusters in the fibroin layer. Robust Ag filaments with localized high density could be formed during such processes, and the LRS of such stable filaments cannot be switched back to HRS, leading to permanent breakdown in the WORM device.

To provide additional insights into the mechanistic study of the RS effect, as well as the exploration of high-performance protein-based RS devices, sericin was also used to study the configurable RS effect. Similar results were obtained as those of fibroin, which are shown in Figures S11–S13 (Supporting Information). Thus, we conclude that the switchable transport among migrating Ag nanoparticles is an universal mechanism underlying the RS operation of such protein-based devices, and this study is helpful for the development of protein-based electronic devices with configurable functionalities.[77]

3. Conclusion

In conclusion, this is the first report of RS devices with configurable functionality based on silk protein. The RS type of the devices can be effectively and exactly controlled by controlling the compliance current in the set process. Memory RS can be triggered by a higher compliance current, while threshold RS can be triggered by a lower compliance current. Furthermore, two types of memory devices, working in random access and WORM modes, can be achieved with the RS effect. The devices with a high resistance OFF/ON ratio of about 10^7 and a long retention time of more than 4500 s have been obtained for the random access memory, whereas the devices with a high resistance OFF/ON ratio of 10^8 and a retention time of more than 10^4 s have been achieved for the WORM memory. Our findings have provided important guidelines for not only the optimization of memory performance, but also the mechanistic study of the RS effect based on biomaterials. The good performance of such protein-based devices suggests that such organic memories complement the conventional inorganic counterparts, and these environmentally friendly biomaterials possess the potential for sustainable electronics and data storage.

4. Experimental Section

The silk fibroin solution used for device synthesis was prepared according to the method described in the literature. *Bombyx mori* cocoons were boiled for 45 min in 0.02 M Na_2CO_3 and rinsed thoroughly with distilled water in order to extract the sericin. The extracted fibroin was dissolved in 9.3 M LiBr solution at 60 °C for 4 h. After that, the obtained solution was subsequently dialyzed in distilled water using the dialysis membrane (MWCO: 3500, Spectrum Laboratories, Inc.) for 72 h. The solution was then centrifuged (9000 rpm) twice and the resultant supernatant was collected and stored at 4 °C. For the preparation of fibroin films, the fibroin solution was first diluted by distilled water to the desired concentrations. For device fabrication, silicon wafers with 280 nm silicon dioxide were used as substrates, which were ultrasonically cleaned in acetone, ethanol, and deionized water, and dried with N_2. A 50 nm Au film with 3 nm Cr adhesion layer was then thermally deposited onto the substrate to act as the bottom electrodes. Thereafter, the aqueous solution of fibroin was spin-coated onto the Au electrodes at 500 rpm for 5 s and 3000 rpm for 45 s and approximately 120 nm fibroin film was formed. Finally, the top Ag electrodes were thermally evaporated onto the device and patterned using a shadow mask. The *I–V* characteristics of the devices were carried out using the Keithley 4200-SCS semiconductor parameter analyzer at room temperature and atmospheric pressure. The depth distribution of Ag in fibroin film was analyzed by time-of-flight secondary ion mass spectrometry (ToF-SIMS). For the sericin-based devices, sericin with molecular weight of 8000 g mol^{-1} (purchased from Aotesi Biotechnology, China) was used as the functional material.

Supporting Information

Supporting Information is available from the Wiley Online Library or from the author.

Acknowledgements

This work was supported by the Singapore National Research Foundation (NRF-RF2009-04) and NTU-A*STAR Silicon Technologies Centre of Excellence under the program Grant No. 11235150003.

Received: April 7, 2015
Published online: May 13, 2015

[1] C. Bettinger, Z. Bao, *Adv. Mater.* **2010**, *22*, 651.
[2] S. Hwang, X. Huang, J. Seo, J. Song, S. Kim, S. Ali, H. Chung, H. Tao, F. Omenetto, Z. Ma, J. Rogers, *Adv. Mater.* **2013**, *25*, 3526.
[3] M. Vladu, E. Glowackib, G. Vossb, S. Bauera, N. Sariciftci, *Mater. Today* **2012**, *15*, 340.
[4] M. Vladu, N. Sariciftci, S. Bauer, *J. Mater. Chem.* **2011**, *21*, 1350.
[5] J. Chang, C. Wang, C. Huang, T. Tsai, T. Guo, T. Wen, *Adv. Mater.* **2011**, *23*, 4077.
[6] N. Amdursky, I. Pecht, M. Sheves, D. Cahen, *J. Am. Chem. Soc.* **2012**, *134*, 18221.
[7] I. Ron, I. Pecht, M. Sheves, D. Cahen, *Acc. Chem. Res.* **2010**, *43*, 945.
[8] I. Ron, L. Sepunaru, S. Itzhakov, T. Belenkova, N. Friedman, I. Pecht, M. Sheves, D. Cahen, *J. Am. Chem. Soc.* **2010**, *132*, 4131.
[9] P. Zalar, D. Kamkar, R. Naik, F. Ouchen, J. Grote, G. Bazan, T. Nguyen, *J. Am. Chem. Soc.* **2011**, *133*, 11010.
[10] Y. Zhang, P. Zalar, C. Kim, S. Collins, G. Bazan, T. Nguyen, *Adv. Mater.* **2012**, *24*, 4255.
[11] Y. Chen, M. Hong, G. Huang, *Nat. Nanotechnol.* **2012**, *7*, 197.
[12] H. Tao, D. Kaplan, F. Omenetto, *Adv. Mater.* **2012**, *24*, 2824.
[13] D. Rockwood, R. Preda, T. Yücel, X. Wang, M. Lovett, D. Kaplan, *Nat. Protoc.* **2011**, *6*, 1612.
[14] E. Mentovich, B. Belgorodsky, I. Kalifa, H. Cohen, S. Richter, *Nano Lett.* **2009**, *9*, 1296.

[15] C. Wang, C. Hsieh, J. Hwang, *Adv. Mater.* **2011**, *23*, 1630.
[16] D. Lin, H. Tao, J. Trevino, J. Mondia, D. Kaplan, F. Omenetto, L. Negro, *Adv. Mater.* **2012**, *24*, 6088.
[17] C. Bettinger, K. Cyr, A. Matsumoto, R. Langer, J. Borenstein, D. Kaplan, *Adv. Mater.* **2007**, *19*, 2847.
[18] D. Kim, J. Viventi, J. Amsden, J. Xiao, L. Vigeland, Y. Kim, J. Blanco, B. Panilaitis, E. Frechette, D. Contreras, D. Kaplan, F. Omenetto, Y. Huang, K. Hwang, M. Zakin, B. Litt, J. Rogers, *Nat. Mater.* **2010**, *9*, 511.
[19] F. Meng, L. Jiang, K. Zheng, C. Goh, S. Lim, H. Hng, J. Ma, F. Boey, X. Chen, *Small* **2011**, *7*, 3016.
[20] H. Wang, F. Meng, B. Zhu, W. Leow, Y. Liu, X. Chen, *Adv. Mater.* **2015**, DOI: 10.1002/adma.201405728.
[21] K. Terabe, T. Hasegawa, T. Nakayama, M. Aono, *Nature* **2005**, *433*, 47.
[22] D. Strukov, G. Snider, D. Stewart, R. Williams, *Nature* **2008**, *453*, 80.
[23] J. Yang, D. Strukov, D. Stewart, *Nat. Nanotechnol.* **2013**, *8*, 13.
[24] J. Seok, S. Song, J. Yoon, K. Yoon, T. Park, D. Kwon, H. Lim, G. Kim, D. Jeong, C. Hwang, *Adv. Funct. Mater.* **2014**, *24*, 5316.
[25] Y. Lai, Y. Wang, Y. Huang, T. Lin, Y. Hsieh, Y. Yang, Y. Chen, *Adv. Funct. Mater.* **2014**, *24*, 1430.
[26] M. Khan, U. Bhansali, M. Almadhoun, I. Odeh, D. Cha, H. Alshareef, *Adv. Funct. Mater.* **2014**, *24*, 1372.
[27] F. Messerschmitt, M. Kubicek, S. Schweiger, J. Rupp, *Adv. Funct. Mater.* **2014**, *24*, 7448.
[28] J. Shang, G. Liu, H. Yang, X. Zhu, X. Chen, H. Tan, B. Hu, L. Pan, W. Xue, R. Li, *Adv. Funct. Mater.* **2014**, *24*, 2171.
[29] Y. Nian, J. Strozier, N. Wu, X. Chen, A. Ignatiev, *Phys. Rev. Lett.* **2007**, *98*, 146403.
[30] K. Szot, W. Speier, G. Bihlmayer, R. Waser, *Nat. Mater.* **2006**, *5*, 312.
[31] J. Jang, F. Pan, K. Braam, V. Subramanian, *Adv. Mater.* **2012**, *24*, 3573.
[32] G. Wen, Z. Ren, D. Sun, T. Zhang, L. Liu, S. Yan, *Adv. Funct. Mater.* **2014**, *24*, 3446.
[33] J. Hou, S. Nonnenmann, W. Qin, D. Bonnell, *Adv. Funct. Mater.* **2014**, *24*, 4113.
[34] J. Ouyang, C. Chu, C. Szmanda, L. Ma, Y. Yang, *Nat. Mater.* **2004**, *3*, 918.
[35] H. Nili, S. Walia, S. Balendhran, D. Strukov, M. Bhaskaran, S. Sriram, *Adv. Funct. Mater.* **2014**, *24*, 6741.
[36] J. Yoon, S. Song, I. Yoo, J. Seok, K. Yoon, D. Kwon, T. Park, C. Hwang, *Adv. Funct. Mater.* **2014**, *24*, 5086.
[37] S. Hahm, N. Kang, W. Kwon, K. Kim, Y. Ko, S. Ahn, B. Kang, T. Chang, J. Lee, M. Ree, *Adv. Mater.* **2012**, *24*, 1062.
[38] S. Han, Y. Zhou, V. A. L. Roy, *Adv. Mater.* **2013**, *25*, 5425.
[39] Q. Liu, J. Sun, H. Lv, S. Long, K. Yin, N. Wan, Y. Li, L. Sun, M. Liu, *Adv. Mater.* **2012**, *24*, 1844.
[40] T. You, Y. Shuai, W. Luo, N. Du, D. Bürger, I. Skorupa, R. Hübner, S. Henker, C. Mayr, R. Schüffny, T. Mikolajick, O. Schmidt, H. Schmidt, *Adv. Funct. Mater.* **2014**, *24*, 3357.
[41] J. Park, S. Lee, J. Lee, K. Yong, *Adv. Mater.* **2013**, *25*, 6423.
[42] M. Min, S. Seo, S. Lee, H. Lee, *Adv. Mater.* **2013**, *25*, 7045.
[43] S. Nau, S. Sax, E. List-Kratochvil, *Adv. Mater.* **2014**, *26*, 2508.
[44] A. Sharma, M. Noman, M. Abdelmoula, M. Skowronski, J. Bain, *Adv. Funct. Mater.* **2014**, *24*, 5522.
[45] Y. Yang, J. Lee, S. Lee, C. Liu, Z. Zhong, W. Lu, *Adv. Mater.* **2014**, *26*, 3693.
[46] S. Ambrogio, S. Balatti, S. Choi, D. Ielmini, *Adv. Mater.* **2014**, *26*, 3885.
[47] W. Lin, S. Liu, T. Gong, Q. Zhao, W. Huang, *Adv. Mater.* **2014**, *26*, 570.
[48] X. Tian, S. Yang, M. Zeng, L. Wang, J. Wei, Z. Xu, W. Wang, X. Bai, *Adv. Mater.* **2014**, *26*, 3649.
[49] H. Yen, C. Chen, G. Liou, *Adv. Funct. Mater.* **2013**, *23*, 5307.
[50] D. Brunel, C. Anghel, D. Kim, S. Tahir, S. Lenfant, A. Filoramo, T. Kontos, D. Vuillaume, V. Jourdain, V. Derycke, *Adv. Funct. Mater.* **2013**, *23*, 5631.
[51] C. Lenser, M. Patt, S. Menzel, A. Köhl, C. Wiemann, C. Schneider, R. Waser, R. Dittmann, *Adv. Funct. Mater.* **2014**, *24*, 4466.
[52] A. Breemen, T. Zaba, V. Khikhlovskyi, J. Michels, R. Janssen, M. Kemerink, G. Gelinck, *Adv. Funct. Mater.* **2015**, *25*, 278.
[53] Y. Hung, W. Hsu, T. Lin, L. Fruk, *Appl. Phys. Lett.* **2011**, *99*, 253301.
[54] Y. Ko, Y. Kim, H. Baek, J. Cho, *ACS Nano* **2011**, *5*, 9918.
[55] M. Hota, M. Bera, B. Kundu, S. Kundu, C. Maiti, *Adv. Funct. Mater.* **2012**, *22*, 4493.
[56] H. Wang, F. Meng, Y. Cai, L. Zheng, Y. Li, Y. Liu, Y. Jiang, X. Wang, X. Chen, *Adv. Mater.* **2013**, *25*, 5498.
[57] F. Meng, B. Sana, Y. Li, Y. Liu, S. Lim, X. Chen, *Small* **2014**, *10*, 277.
[58] M. Uenuma, T. Ban, N. Okamoto, B. Zheng, Y. Kakihara, M. Horita, Y. Ishikawa, I. Yamashita, Y. Uraoka, *RSC Adv.* **2013**, *3*, 18044.
[59] C. Mukherjee, M. Hota, D. Naskar, S. Kundu, C. Maiti, *Phys. Status Solidi A* **2013**, *210*, 1797.
[60] N. Gogurla, S. Mondal, A. Sinha, A. Katiyar, W. Banerjee, S. Kundu, S. Ray, *Nanotechnology* **2013**, *24*, 345202.
[61] N. Hosseini, J. Lee, *ACS Nano* **2015**, *9*, 419.
[62] L. He, Z. Liao, H. Wu, X. Tian, D. Xu, G. Cross, G. Duesberg, I. Shvets, D. Yu, *Nano Lett.* **2011**, *11*, 4601.
[63] S. Chang, J. Lee, S. Chae, S. Lee, C. Liu, B. Kahng, D. Kim, T. Noh, *Phys. Rev. Lett.* **2009**, *102*, 026801.
[64] H. Peng, Y. Li, W. Lin, Y. Wang, X. Gao, T. Wu, *Sci. Rep.* **2012**, *2*, 442.
[65] H. Sun, Q. Liu, C. Li, S. Long, H. Lv, C. Bi, Z. Huo, L. Li, M. Liu, *Adv. Funct. Mater.* **2014**, *24*, 5679.
[66] M. Lee, Y. Park, D. Suh, E. Lee, S. Seo, D. Kim, R. Jung, B. Kang, S. Ahn, C. Lee, D. Seo, Y. Cha, I. Yoo, J. Kim, B. Park, *Adv. Mater.* **2007**, *19*, 3919.
[67] J. Liu, Z. Yin, X. Cao, F. Zhao, L. Wang, W. Huang, H. Zhang, *Adv. Mater.* **2013**, *25*, 233.
[68] Y. Hirose, H. Hirose, *J. Appl. Phys.* **1976**, *47*, 2767.
[69] R. Waser, R. Dittmannn, G. Staikov, K. Szot, *Adv. Mater.* **2009**, *21*, 2632.
[70] M. A. Lampert, P. Mark, *Current Injection in Solids*, Academic, New York **1970**.
[71] D. Shang, Q. Wang, L. Chen, R. Dong, X. Li, W. Zhang, *Phys. Rev. B: Condens. Matter* **2006**, *73*, 245427.
[72] Q. Zuo, S. Long, Q. Liu, S. Zhang, Q. Wang, Y. Li, Y. Wang, M. Liu, *J. Appl. Phys.* **2009**, *106*, 073724.
[73] Y. Yang, P. Gao, G. Siddharth, T. Chang, X. Pan, W. Lu, *Nat. Commun.* **2012**, *3*, 372.
[74] A. Sawa, *Mater. Today* **2008**, *11*, 28.
[75] Y. M. Du, A. Kumar, H. Pan, K. Y. Zeng, S. J. Wang, P. Wang, A. T. S. Wee, *AIP Adv.* **2013**, *3*, 082107.
[76] S. Wu, X. Luo, S. Turner, H. Peng, W. Lin, J. Ding, A. David, B. Wang, G. V. Tendeloo, J. Wang, T. Wu, *Phys. Rev. X* **2013**, *3*, 041027.
[77] F. Meng, Y. Hervault, Q. Shao, B. Hu, L. Norel, S. Rigaut, X. Chen, *Nat. Commun.* **2014**, *5*, 3023.